

Research Article

A MEMS-IMU Assisted BDS Triple-Frequency Ambiguity Resolution Method in Complex Environments

Junbing Cheng, Deng-ao Li , and Jumin Zhao 

College of Information and Computer, Taiyuan University of Technology, Jinzhong 03600, China

Correspondence should be addressed to Deng-ao Li; lidengao@tyut.edu.cn

Received 12 July 2018; Revised 11 October 2018; Accepted 28 October 2018; Published 4 December 2018

Academic Editor: Xiaoliang Jin

Copyright © 2018 Junbing Cheng et al. This is an open access article distributed under the Creative Commons Attribution License, which permits unrestricted use, distribution, and reproduction in any medium, provided the original work is properly cited.

Emerging technologies such as smart cities and unmanned vehicles all need Global Navigation Satellite Systems (GNSS) to provide high-precision positioning and navigation services. Fast and reliable carrier phase ambiguity resolution (AR) is a prerequisite for high-precision positioning. The poor satellite geometry and severe multipath effect caused by Beidou Navigation Satellite System (BDS) signal occlusion and reflection in complex environments will degrade the AR performance. In this contribution, a fast triple-frequency AR method combining Microelectromechanical System-Inertial Measurement Unit (MEMS-IMU) and BDS is proposed. First, the Extra-Wide Lane (EWL) ambiguity is fixed with the positioning parameters of MEMS-IMU instead of the pseudorange. Then, the phase noise variance of Narrow Lane (NL) observation is obtained from ambiguity-fixed EWL observation to reduce the total noise level of NL observation, and the NL ambiguity can be reliably fixed, and the BDS positioning result is obtained. Finally, the BDS positioning result is used as the posterior measurement of the extended Kalman filter to update the MEMS-IMU positioning parameters to form the coupling loop of MEMS-IMU and BDS. The data of urban road vehicle experiments were collected to verify the feasibility and effectiveness of the proposed algorithm. Results show that MEMS-IMU can speed up AR, and reduction of total noise level can significantly improve the reliability of AR.

1. Introduction

With the indepth development of information technology, next-generation information technologies such as the Internet of Things (IOT), smart city, and unmanned vehicle all need high-accuracy time and space service support. The Global Navigation Positioning System (GNSS) can provide reliable high-precision positioning and timing services. The key to realizing high-precision positioning for GNSS is to quickly and reliably resolve integer carrier phase ambiguity [1]. However, GNSS signals are obstructed and reflected by obstacles such as high-rise buildings and tunnels in complex environments, causing serious multipath effects and poor satellite geometry, which have become the great challenge to correctly resolve the integer ambiguity. Severe multipath effects reduce the quality of the observations, and poor satellite geometry increases the correlation between the observations, making it more difficult to search for integer ambiguities, all of which degrade the performance of Ambiguity Resolution (AR) and positioning [2]. Teunissen

adopted the “Z” transform to degrade the correlation between the float ambiguities to speed up the fixation of ambiguities, which is known as the Least squares AMBiguity Decorelation Adjustment (LAMBDA) method [3]; Teunissen and Odolinski also proposed that Multiple GNSS combinations increase the number of available satellites to improve satellite geometry and improve GNSS positioning performance in harsh environments [4, 5]. There are also studies based on the principle that positioning can be achieved with only four available satellites and selecting high-quality observations for Partial Ambiguity Resolution (PAR) to reduce the negative effects of complex environment on positioning results [6, 7]. These studies are based on single-frequency or dual-frequency observations AR methods. Tang et al. have shown that triple-frequency observations have better AR performance than dual-frequency observations [8].

The Chinese Beidou Navigation Satellite System (BDS) constellation transmits observations at three frequencies (B1, B2, and B3), including pseudorange and carrier phase observations [9]. This provides many advantages for the AR,

because the triple-frequency phase carrier observations can form a virtual observation with long wavelength, small atmospheric delay and low noise through linear combination [10]. The triple-frequency linear combination not only increases redundancy of the observations but also improves the real-time and reliability of the AR. Forssell and Vollath first investigated the method of achieving high-accuracy positioning by combining triple-frequency observations and proposed the classic Three-Carrier Ambiguity Resolution (TCAR) method [11, 12]. Hatch et al. also proposed a triple-frequency AR method-Cascading Integer Resolution (CIR) [13]. The TCAR and CIR essentially select the three independent combinations, first fix the Extra-Wide Lane (EWL) ambiguity with pseudorange, then fix the Wide-Lane (WL) ambiguity with ambiguity-resolved EWL observation, and finally fix the Narrow Lane (NL) ambiguity with ambiguity-resolved WL observation, which resolves ambiguity step by step in a cascading manner and obtain high-precision positioning solutions. These two early three-frequency AR methods are simple to calculate, but for medium-long baseline or complex environments such as urban canyons, the AR performance will decrease due to the weak model strength. Feng proposed the GB (geometry-based)-TCAR method and selected three-frequency combined observations with small ionospheric scale factor to eliminate the influence of ionospheric delay for the medium-long baseline [14]. On the basis of eliminating the influence of ionospheric delay, Li et al. proposed the GIF (geometry-free and ionosphere-free-) TCAR model that can simultaneously eliminate the influence of tropospheric delay, so that the AR performance is independent of the baseline length [15]. Zhao et al. took into account the principle of noise minimization under the premise of the geometry-free and ionosphere-free, further improved the traditional TCAR method, and improved the success rate of AR for medium and long baselines [16]. Tian et al. used the relationship of ionospheric scale factor between the EWL and the NL observations to address the issue that the ionospheric delay at the mid-to-long baseline cannot be eliminated by double differences (DD) [17]. Lou et al. analyzed the effects of code bias variations induced by three types of BDS satellites on AR of EWL, WL, and NL combinations and propose to model the single-differenced fractional cycle bias with widespread ground stations [18]. Deng et al. proposed an optimal combination of triple-frequency pseudocode and carrier phase driven by models and data and took full advantage of the low noise characteristics of B3 to reduce the total noise level [19]. The above methods improve the traditional TCAR method from different aspects and improve the AR and positioning performance.

However, the EWL ambiguity is fixed by pseudorange, and the multipath effect caused by the complex environment will reduce the AR performance of the traditional TCAR and its derivative methods. Obviously, completely eliminating code multipath error will improve AR performance. Feng-Yu Chu et al. proposed a method to resolve ambiguities using only triple-frequency carrier phase observations, completely eliminating the effects of code multipath, and pointed out that the positioning performance is still affected by the carrier phase multipath [20]. The Inertial Navigation System (INS)

not only has strong autonomy but also can output short-time high-precision positioning parameters at high frequency [21]. The disadvantage is that the error accumulates over time and it has strong complementary with GNSS. Grejner-Brzezinska et al. firstly proposed a Global Positioning System (GPS)/INS tightly coupled model and described in detail the process of implementing integrated navigation system through the Kalman filter [22]. Godha et al. showed that GPS/INS integrated system can still output effective positioning information when GPS signal is interrupted and pointed out that the INS has great potential in vehicle navigation applications [23]. These studies mainly coupled pseudorange and Doppler observation level integrated system, because the accuracy of the pseudorange itself is not very high, and positioning accuracy can only be in the meter level. Liu et al. proposed a GPS/INS tightly coupled ambiguity fixed solution algorithm, and achieved a centimeter-level quick positioning [24]. Han et al. not only improved the accuracy of the float ambiguity by coupling INS but also used the advantages of GPS and BDS combination to reduce the impact of large-error observations on the AR performance by PAR method [25]. Li et al. proposed a strategy for detecting and rejecting observations with large errors to reduce the adverse effect of code multipath [26].

In fact, the original carrier wavelength of GNSS is about 20cm, while the prediction error of some low-cost Microelectromechanical System-Inertial Measurement Unit (MEMS-IMU) in within 1 epoch (1s) of GNSS for geometric distance is more than half of the original carrier wavelength [27]. Obviously, the accuracy of the low-cost MEMS-IMU does not meet the requirement to fix the original carrier ambiguity by rounding. The EWL observations formed by the linear combination of the triple-frequency original carrier phase observations have a wavelength of up to 5m, which can make the accuracy of the low-cost MEMS-IMU enough to meet the fixed ambiguity requirement. In addition, pseudoranges in complex environment such as urban canyon are affected by severe multipath effects, with large errors, sometimes as high as 4m [28]. It is difficult to fix the ambiguity, even the EWL ambiguity. While positioning parameters of the MEMS-IMU have relatively high accuracy in a short time, using the MEMS-IMU corresponding geometric distance instead of the pseudorange to fix the EWL ambiguity will increase the fixed success rate of ambiguity. According to error propagation theory, it also has a positive impact on the fixation of WL ambiguities.

We investigated the causes of AR performance degradation in complex environments and improved the first and third steps of the traditional TCAR method. The high quality positioning parameters of the MEMS-IMU are used to assist in fixing the EWL ambiguity, and the NL ambiguity is reliably fixed after the total noise variance is reduced. The MEMS-IMU and BDS are loosely coupled at the centimeter level to achieve high-precision positioning by Extended Kalman Filter (EKF).

The rest of this paper is organized as follows. Section 2 first introduced the general model of the traditional TCAR and the two limiting factors in a complex environment, and then the innovative solutions was given in two steps.

The source of the data and the parameters of the relevant experimental equipment are described in Section 3. Section 4 illustrates the difference between the open sky and the urban canyon through comparative experiments and validates the effectiveness of the proposed algorithm based on the innovations. Section 5 is the conclusion and outlook.

2. Methods

2.1. The TCAR General Models and Limiting Factors in Complex Environments. In the open sky environment, the traditional TCAR method can efficiently resolve the triple-frequency ambiguity due to high-precision observations. However, in a complex environment where the BDS signal occluded and reflected, the severe multipath effect makes it difficult for the traditional TCAR method to reliably and instantaneously resolve the triple-frequency ambiguity.

2.1.1. Triple-Frequency Observations and Basic Formulas. The observation formula of the BDS carrier phase and pseudorange can be expressed as

$$\Phi = \rho + H + O + T - I + c(dt^s - dt_r) + \lambda \cdot N + \varepsilon_\Phi \quad (1)$$

$$P = \rho + H + O + T + I + c(dt^s - dt_r) + \varepsilon_P \quad (2)$$

where Φ and P denote the pseudorange and carrier phase, respectively, ρ denotes the geometric distance between the satellite and the receiver, H and O denote the receiver hardware delay and satellite orbital error respectively, T and I denote the troposphere and ionosphere delay, respectively. c denotes the speed of light propagation in a vacuum, dt^s and dt_r denote the satellite clock error and receiver clock error, respectively, and ε_P and ε_Φ denote the pseudorange and carrier phase other errors including multipath, respectively.

For short baselines (baseline length < 20km), the spatiotemporal correlation between observations is strong. After intersatellite difference and interreceiver difference, the satellite clock error, the receiver clock error, and the hardware delay are completely eliminated, the tropospheric error, the ionospheric error, and the satellite orbit error are also greatly weakened and can be ignored. Therefore, after the double differenced (DD) operation, the observation formula is

$$\Delta\nabla\Phi = \Delta\nabla\rho + \lambda \cdot \Delta\nabla N + \varepsilon_{\Delta\nabla\Phi} \quad (3)$$

$$\Delta\nabla P = \Delta\nabla\rho + \varepsilon_{\Delta\nabla P} \quad (4)$$

where $\Delta\nabla\Phi$ and $\Delta\nabla P$, respectively, represent the DD carrier phase and pseudorange, $\Delta\nabla\rho$ represents the DD geometric distance, $\varepsilon_{\Delta\nabla P}$ and $\varepsilon_{\Delta\nabla\Phi}$ represent the DD pseudorange and carrier phase other errors, respectively, and $\Delta\nabla N$ represents DD integer ambiguity.

The triple-frequency DD observations can form virtual observations with various favorable characteristics for AR. The linear combination of triple-frequency DD observations can be expressed as [14]

$$\Delta\nabla\Phi_{(i,j,k)} = \frac{i \cdot f_1 \Delta\nabla\Phi_1 + j \cdot f_2 \Delta\nabla\Phi_2 + k \cdot f_3 \Delta\nabla\Phi_3}{i \cdot f_1 + j \cdot f_2 + k \cdot f_3} \quad (5)$$

$$\Delta\nabla\varphi_{(i,j,k)} = i \cdot \varphi_1 + j \cdot \varphi_2 + k \cdot \varphi_3 \quad (6)$$

$$\Delta\nabla P_{(i,j,k)} = \frac{i \cdot f_1 \Delta\nabla P_1 + j \cdot f_2 \Delta\nabla P_2 + k \cdot f_3 \Delta\nabla P_3}{i \cdot f_1 + j \cdot f_2 + k \cdot f_3} \quad (7)$$

where $\Delta\nabla\Phi_{(i,j,k)}$ and $\Delta\nabla P_{(i,j,k)}$ represent the observations of the carrier phase and pseudorange combined in meter, respectively; $\Delta\nabla\varphi_{(i,j,k)}$ is the observations of the carrier phase in cycle, i , j , and k are the combined coefficients corresponding to the three frequencies of BDS, respectively, and they are all integers; f_i represents the frequency of the three original carriers; $\Delta\nabla\Phi_i$ and $\Delta\nabla P_i$ represent the original carrier phase and pseudorange observations in meters and φ_i represents the original carrier phase observations in cycle. The frequency, wavelength, and integer ambiguity of the carrier phase combination observations are as follows:

$$f_{(i,j,k)} = i \cdot f_1 + j \cdot f_2 + k \cdot f_3 \quad (8)$$

$$\lambda_{(i,j,k)} = \frac{c}{i \cdot f_1 + j \cdot f_2 + k \cdot f_3} \quad (9)$$

$$\Delta\nabla N_{(i,j,k)} = i \cdot \Delta\nabla N_1 + j \cdot \Delta\nabla N_2 + k \cdot \Delta\nabla N_3 \quad (10)$$

where N_i represents the original carrier phase integer ambiguity.

The combined observations of DD pseudorange and carrier phase can be expressed as

$$\Delta\nabla\Phi_{(i,j,k)} = \Delta\nabla\rho + \lambda_{(i,j,k)} \cdot \Delta\nabla N_{(i,j,k)} + \varepsilon_{\Delta\nabla\Phi_{(i,j,k)}} \quad (11)$$

$$\Delta\nabla P_{(i,j,k)} = \Delta\nabla\rho + \varepsilon_{\Delta\nabla P_{(i,j,k)}} \quad (12)$$

The carrier phase combination observations are only mathematically combined and their noise originates from the original carrier noise. Assuming that the noise at the three frequencies of the BDS is equal and uncorrelated, equal to $\delta_{\Delta\nabla\Phi}^2$, then

$$\delta_{\Delta\nabla\Phi_1}^2 = \delta_{\Delta\nabla\Phi_2}^2 = \delta_{\Delta\nabla\Phi_3}^2 = \delta_{\Delta\nabla\Phi}^2 \quad (13)$$

$$\begin{aligned} \delta_{\Delta\nabla\Phi_{(i,j,k)}}^2 &= \frac{(i \cdot f_1)^2 + (j \cdot f_2)^2 + (k \cdot f_3)^2}{(i \cdot f_1 + j \cdot f_2 + k \cdot f_3)^2} \cdot \delta_{\Delta\nabla\Phi}^2 \\ &= \mu_{(i,j,k)}^2 \cdot \delta_{\Delta\nabla\Phi}^2 \end{aligned} \quad (14)$$

where $\mu_{(i,j,k)}$ is the phase noise factor (PNF) of combination observation. The ionospheric scale factor (ISF) $\beta_{(i,j,k)}$ of first-order ionospheric delay for the combination observations with respect to BI is expressed as

$$\beta_{(i,j,k)} = \frac{\sqrt{(i \cdot f_1)^2 + (j \cdot f_2)^2 + (k \cdot f_3)^2}}{i \cdot f_1 + j \cdot f_2 + k \cdot f_3} \quad (15)$$

2.1.2. The Traditional TCAR Method. The BDS triple-frequency linear combination can form a lot of virtual observations. Table 1 shows some commonly used BDS triple-frequency combinations. The (0,1,-1) combination with the longest wavelength is considered as EWL; the (1,-1,0) combination with a slightly shorter wavelength is considered as WL; the (4,0,-3) combination with the shortest wavelength is considered as NL.

TABLE 1: Commonly used BDS triple-frequency combinations and related parameters.

(i, j, k)	$\lambda_{(i,j,k)}$ (m)	$\beta_{(i,j,k)}$	$\mu_{(i,j,k)}$
(1,0,0)	0.192	1	1
(0,1,0)	0.248	1.672	1
(0,0,1)	0.236	1.515	1
(0,-1,1)	4.884	-1.592	28.529
(1,-1,0)	0.847	-1.293	5.575
(4,0,-3)	0.123	0.1972	2.9984

The traditional TCAR method is a method that is independent of the satellite geometry, namely the GF- (geometry-free) TCAR method. The three combined observations are fixed by the rounding method.

Step 1. EWL ambiguity

$$\Delta\nabla\widehat{N}_{(i_e, j_e, k_e)} = \frac{\Delta\nabla P}{\lambda_{(i_e, j_e, k_e)}} - \Delta\nabla\varphi_{(i_e, j_e, k_e)} + \frac{\varepsilon_{\Delta\nabla P} - \varepsilon_{\Delta\nabla\Phi_{(i_e, j_e, k_e)}}}{\lambda_{(i_e, j_e, k_e)}} \quad (16)$$

$$\Delta\nabla\check{N}_{(i_e, j_e, k_e)} = \text{round} \left[\Delta\nabla\widehat{N}_{(i_e, j_e, k_e)} \right] \quad (17)$$

where $\Delta\nabla\widehat{N}_{(i_e, j_e, k_e)}$ and $\Delta\nabla\check{N}_{(i_e, j_e, k_e)}$ represent the EWL float ambiguity and integer ambiguity, respectively, and $\text{round}[\cdot]$ represents the rounding operation.

Step 2. WL ambiguity:

$$\Delta\nabla\widehat{N}_{(i_w, j_w, k_w)} = \frac{\Delta\nabla\Phi_{(i_e, j_e, k_e)} - \lambda_{(i_e, j_e, k_e)} \cdot \Delta\nabla\check{N}_{(i_e, j_e, k_e)}}{\lambda_{(i_w, j_w, k_w)}} - \Delta\nabla\varphi_{(i_w, j_w, k_w)} + \frac{\varepsilon_{\Delta\nabla\Phi_{(i_e, j_e, k_e)}} - \varepsilon_{\Delta\nabla\Phi_{(i_w, j_w, k_w)}}}{\lambda_{(i_w, j_w, k_w)}} \quad (18)$$

$$\Delta\nabla\check{N}_{(i_w, j_w, k_w)} = \text{round} \left[\Delta\nabla\widehat{N}_{(i_w, j_w, k_w)} \right] \quad (19)$$

Step 3. NL ambiguity:

$$\Delta\nabla\widehat{N}_{(i_n, j_n, k_n)} = \frac{(\Delta\nabla\Phi_{(i_w, j_w, k_w)} - \lambda_{(i_w, j_w, k_w)} \Delta\nabla\check{N}_{(i_w, j_w, k_w)})}{\lambda_{(i_n, j_n, k_n)}} - \Delta\nabla\varphi_{(i_n, j_n, k_n)} + \frac{\varepsilon_{\Delta\nabla\Phi_{(i_w, j_w, k_w)}} - \varepsilon_{\Delta\nabla\Phi_{(i_n, j_n, k_n)}}}{\lambda_{(i_n, j_n, k_n)}} \quad (20)$$

$$\Delta\nabla\check{N}_{(i_n, j_n, k_n)} = \text{round} \left[\Delta\nabla\widehat{N}_{(i_n, j_n, k_n)} \right] \quad (21)$$

The traditional TCAR and its derivative methods use pseudorange to fix EWL or WL ambiguity. As can be seen from formula (16), the accuracy of the EWL float ambiguity

depends on the accuracy of the pseudocode and EWL observations and the influence of the pseudorange error is greater because the pseudorange error is generally considered to be 100 times the carrier phase error:

$$\delta_{\Delta\nabla\check{N}_{(i_e, j_e, k_e)}} = \frac{\sqrt{\delta_{\Delta\nabla P_{(i_p, j_p, k_p)}}^2 + \delta_{\Delta\nabla\Phi_{(i_e, j_e, k_e)}}^2}}{\lambda_{(i_e, j_e, k_e)}} \quad (22)$$

In the open sky environment, the accuracy of pseudorange and carrier phase is relatively high, and the accuracy of virtual observations is also relatively high. The BDS triple-frequency ambiguity can be resolved instantaneously and reliably by the traditional TCAR method.

2.1.3. *Limiting Factors of Traditional TCAR Method in Complex Environments.* For short baselines, the main error source of BDS positioning in complex environment is the multipath error, especially code multipath error. The multipath effect reduces the accuracy of the pseudorange and increases the convergence time of the pseudorange fixed EWL ambiguity and will bring the error to the fixed WL ambiguity.

The multipath effect will not only increase the code error but also increase the carrier phase error. Under the condition that the reflection coefficient is 1, the carrier phase multipath error is at most 0.25 wavelengths [29]. In a complex environment, the signal may be reflected by multiple obstacles to accumulate the error. Then DD and linear combination, the phase multipath error further expands. For NL observation wavelengths, the phase multipath error is relatively large so that NL ambiguities are difficult to fix by rounding.

2.2. *MEMS-IMU Fixed EWL Ambiguity.* The fixed speed of ambiguity integer solution depends on the size of the float ambiguity search space, and the ambiguity search space depends on the float ambiguity variance covariance matrix [3]:

$$W \propto \frac{\delta_P}{n\lambda} \quad (23)$$

where W denotes the ambiguity search space, δ_P denotes the pseudorange precision, λ denotes the wavelength, n denotes the number of epochs, and \propto denotes the proportional relationship.

Among the three factors affecting the float ambiguity search space, n cannot be expanded due to the real-time requirements of positioning, λ has been expanded by the triple-frequency combination to form EWL. The multipath effect seriously degrades the accuracy of pseudorange, while the MEMS-IMU has a relatively high accuracy in a short time. The geometric distance corresponding to the MEMS-IMU instead of the pseudorange reduces δ_P to further narrow the ambiguity search space. After the positioning parameters of MEMS-IMU are transformed by the coordinate system, the corresponding geometric distance of the MEMS-IMU can be obtained from the satellite coordinates.

2.2.1. *MEMS-IMU Dynamic Model.* In this study, the loosely coupled form of MEMS-IMU and BDS is realized by

extended Kalman filter. Compared with the tightly coupled form, the loosely coupled form has a simple structure and a small amount of computation, which helps to improve the real-time of AR. A navigation system state error model based on the MEMS-IMU attitude angle is established [30]. The attitude angle error model can be expressed as

$$\delta \dot{r}^n = -\omega_{en}^n \times \delta r^n + \delta v^n \quad (24)$$

$$\delta \dot{v}^n = -(2\omega_{ie}^n + \omega_{en}^n) \times \delta v^n - \delta \psi^n \times f^n + \nabla \quad (25)$$

$$\delta \dot{\psi}^n = -(\omega_{ie}^n + \omega_{en}^n) \times \delta \psi^n + \varepsilon \quad (26)$$

Take into account the state incremental error, the error of the lever arm a total of 24 error terms characterization of the system state:

$$\begin{aligned} X_{nav} &= [\delta r_N \ \delta r_E \ \delta r_D \ \delta v_N \ \delta v_E \ \delta v_D \ \delta \psi_N \ \delta \psi_E \ \delta \psi_D]^T \\ X_{acc} &= [\nabla_{bx} \ \nabla_{by} \ \nabla_{bz} \ \nabla_{fx} \ \nabla_{fy} \ \nabla_{fz}]^T \\ X_{gyro} &= [\varepsilon_{bx} \ \varepsilon_{by} \ \varepsilon_{bz}]^T \\ X_{ant} &= [\delta L_{bx} \ \delta L_{by} \ \delta L_{bz}]^T \\ X_{grav} &= [\delta g_N \ \delta g_E \ \delta g_D]^T \end{aligned} \quad (27)$$

where X_{nav} is 9 navigation errors (3 position errors, 3 velocity errors, and 3 platform angle errors); X_{acc} is 3 acceleration bias errors and 3 scale factor errors; X_{gyro} is 3 gyro bias errors; X_{ant} is 3 arm effect error, and X_{grav} is 3 gravity acceleration errors. Establish the system state equation in the geographic coordinate system (e-system):

$$X_k = \Theta_{k-1} X_{k-1} + w_{k-1} \quad (28)$$

The equation expands to the following form:

$$\begin{aligned} & \begin{bmatrix} \dot{X}_{nav} \\ \dot{X}_{acc} \\ \dot{X}_{gyro} \\ \dot{X}_{grav} \\ \dot{X}_{ant} \end{bmatrix} \\ &= \begin{bmatrix} F_{11} (9 \times 9) & F_{12} (9 \times 6) & F_{13} (9 \times 3) & F_{14} (9 \times 3) & 0 \\ 0 & F_{22} (6 \times 6) & 0 & 0 & 0 \\ 0 & 0 & F_{33} (3 \times 3) & 0 & 0 \\ 0 & 0 & 0 & F_{44} (3 \times 3) & 0 \\ 0 & 0 & 0 & 0 & 0 \end{bmatrix} \quad (29) \\ & \cdot \begin{bmatrix} X_{nav} \\ X_{acc} \\ X_{gyro} \\ X_{grav} \\ X_{ant} \end{bmatrix} + \begin{bmatrix} w_{nav} \\ w_{acc} \\ w_{gyro} \\ w_{grav} \\ 0 \end{bmatrix} \end{aligned}$$

$$\begin{aligned} F_{11} &= \begin{bmatrix} -\omega_{en}^n \times & I_{3 \times 3} & 0_{3 \times 3} \\ F_{up} & -(\omega_{en}^n + 2\omega_{ie}^n) & f^b \times \\ 0_{3 \times 3} & 0_{3 \times 3} & -(\omega_{en}^n + \omega_{ie}^n) \times \end{bmatrix}, \\ F_{up} &= \begin{bmatrix} -\frac{g}{R_e} & 0 & 0 \\ 0 & -\frac{g}{R_e} & 0 \\ 0 & 0 & -\frac{2g}{R_e} \end{bmatrix}, \\ F_{12} &= \begin{bmatrix} 0_{3 \times 3} & 0_{3 \times 3} \\ C_b^n & C_b^n \cdot \text{diag}(f_b) \\ 0_{3 \times 3} & 0_{3 \times 3} \end{bmatrix}, \\ F_{13} &= \begin{bmatrix} 0_{3 \times 3} \\ 0_{3 \times 3} \\ -C_b^n \end{bmatrix}, \\ F_{14} &= \begin{bmatrix} 0_{3 \times 3} \\ I_{3 \times 3} \\ 0_{3 \times 3} \end{bmatrix}, \\ F_{22} &= \text{diag}[-\tau_{\nabla bx} \ -\tau_{\nabla by} \ -\tau_{\nabla bz} \ -\tau_{\nabla fx} \ -\tau_{\nabla fy} \ -\tau_{\nabla fz}], \\ F_{33} &= \text{diag}[-\tau_{\varepsilon bx} \ -\tau_{\varepsilon by} \ -\tau_{\varepsilon bz}], \\ F_{44} &= \text{diag}[-\tau_{gN} \ -\tau_{gE} \ -\tau_{gD}] \end{aligned} \quad (30)$$

where Θ is the state transition matrix of the system; w_{nav} , w_{acc} , w_{gyro} , and w_{grav} are kinetic white Gaussian noise vectors; subscripts N, E, and D are navigational coordinate systems (n-system); subscripts b_x , b_y , and b_z are carrier coordinate systems (b-system); g is the constant of gravity acceleration, R_e is the sum of the height of the carrier and the radius of the earth; δr is the MEMS-IMU position error vector; δv is the MEMS-IMU velocity error vector; $\delta \psi$ is the attitude error vector; ∇ is the acceleration error vector; ε is the gyro drift error vector; ω_{en}^n is the n-system transfer rate; ω_{ie}^n is the rotation rate of the earth in n-system; C_b^n is a b-system to a n-system rotation matrix; f^b is the accelerometer specific force vector; $\tau_{\nabla b}$ is the accelerometer bias error; τ_g is the first order Markov process of the gravity model.

2.2.2. Measurement Model. After the AR is completed, the carrier phase observation can be converted to a high-accuracy BDS positioning result. Considering the deviation between the BDS antenna phase center and the MEMS-IMU reference center, in the e-system, the antenna phase center can be expressed as

$$r_{BDS} = r_{INS}^{BDS} + C_b^e L_b \quad (31)$$

where r_{BDS} is the BDS positioning result, r_{INS}^{BDS} is the positioning parameter of the MEMS-IMU in the b-system, C_b^e is the conversion matrix from the b-system to the e-system, and L_b is the arm length. Then, the conversion between the e-system and the b-system can be realized by the formula (31).

Because the integrated navigation system is loosely coupled, the BDS corrects the accumulated error of the MEMS-IMU over time at the positioning result level. The r_{INS}^{BDS} obtained from r_{BDS} is used as a posterior measurement of the EKF to correct the positioning parameters of the MEMS-IMU.

2.2.3. MEMS-IMU Corresponding Geometric Distance Instead of Pseudorange. The geometrical distance can be calculated from the positioning parameters output from the MEMS-IMU and the satellite coordinates obtained from the BDS precision satellite orbit products:

$$\begin{aligned} \rho_{INS} &= \|r^s - r_{BDS}\| \\ &= \sqrt{(X^s - X_{BDS})^2 + (Y^s - Y_{BDS})^2 + (Z^s - Z_{BDS})^2} \end{aligned} \quad (32)$$

where ρ_{INS} denotes the geometric distance corresponding to the MEMS-IMU positioning parameters, $r^s(X^s, Y^s, Z^s)$ denotes the satellite coordinates obtained by the satellite precision orbital products, $r_{BDS}(X_{BDS}, Y_{BDS}, Z_{BDS})$ denotes the phase center position of the BDS receiver antenna from the EKF, and the accuracy of $\delta_{\rho_{INS}}$ is estimated by an empirical formula [31]:

$$\delta_{\rho_{INS}} = \sqrt{\left(gB_{gyro} \frac{t^3}{6}\right)^2 + \left(B_{acc} \frac{t^2}{2}\right)^2} \quad (33)$$

where t denotes the error cumulative time of the MEMS-IMU, g denotes the gravitational acceleration, and B_{gyro} denotes the gyro bias; B_{acc} denotes the accelerometer bias. The prediction error of the low-cost MEMS-IMU geometric distance in one epoch of BDS is generally less than the code multipath error in complex environments. The pseudorange of the first step in the traditional TCAR method is replaced by ρ_{INS} to accelerate the fixed speed of EWL ambiguity:

$$\begin{aligned} \Delta \nabla \widehat{N}_{(i_e, j_e, k_e)} &= \frac{\Delta \nabla \rho_{INS}}{\lambda_{(i_e, j_e, k_e)}} - \Delta \nabla \varphi_{(i_e, j_e, k_e)} \\ &+ \frac{\varepsilon_{\Delta \nabla \rho_{INS}} - \varepsilon_{\Delta \nabla \varphi_{(i_e, j_e, k_e)}}}{\lambda_{(i_e, j_e, k_e)}} \end{aligned} \quad (34)$$

Obviously, the accuracy of the EWL float ambiguity is greatly improved, so that the EWL ambiguity can be fixed by rounding. Due to the high accuracy of ρ_{INS} and the long wavelength of the WL, the WL ambiguity can also be fixed by rounding. However, the NL observation has a very small wavelength and is even smaller than the original carrier. Due to the effects of carrier phase multipath errors in complex environments, the fixed success rate of NL ambiguity is relatively low.

2.3. Reliable Fixing of NL Ambiguity. The fixation of NL ambiguity is the final step of the TCAR method and the key to achieving high-precision positioning. Based on the PNF relationship between EWL and NL observations, the phase noise variance of the NL observation is obtained from the ambiguity-fixed EWL observation to reduce the total noise of the NL observation, and the accuracy of float ambiguity and the ambiguity fixed success rate are improved.

2.3.1. Reduce the Total Noise Level of NL Observations. The error sources of combined observations mainly include ionospheric delay error, tropospheric delay error, and other errors (mainly phase multipath error) [14]. Then, the total noise level of the combined observations can be expressed as

$$\sigma_{TN}^2 = \beta_{(i,j,k)}^2 \sigma_{\Delta \nabla \delta I, \Phi_1}^2 + \mu_{(i,j,k)}^2 \sigma_{\Delta \nabla \Phi}^2 + \sigma_{\Delta \nabla T}^2 \quad (35)$$

where σ_{TN}^2 represents the total noise level, $\sigma_{\Delta \nabla \delta I, \Phi_1}^2$ represents the ionospheric delay error of B1, and $\sigma_{\Delta \nabla T}^2$ represents tropospheric delay error. For the short baseline, both ionospheric delay error and tropospheric delay errors are negligible due to strong temporal and spatial correlation. Therefore, the main error source of the ambiguity-fixed EWL observation is the noise error including the phase multipath, and according to (14), the noise variance of the NL observations is

$$\sigma_{\Delta \nabla \Phi_{(i_n, j_n, k_n)}}^2 = \frac{\mu_{(i_n, j_n, k_n)}^2}{\mu_{(i_e, j_e, k_e)}^2} \sigma_{\Delta \nabla \Phi_{(i_e, j_e, k_e)}}^2 \quad (36)$$

Substituting the obtained $\sigma_{\Delta \nabla \Phi_{(i_n, j_n, k_n)}}^2$ into formula (35) can significantly reduce the total noise level of the NL observations:

$$\sigma_{TN \Delta \nabla \Phi_{(i_n, j_n, k_n)}}^2 = \sigma_{TN \Delta \nabla \Phi_{(i_n, j_n, k_n)}}^2 - \sigma_{\Delta \nabla \Phi_{(i_n, j_n, k_n)}}^2 \quad (37)$$

The reduced total error level can be obtained according to equation (37). The AR success rate is determined by the mean bias and the variance [32]:

$$\begin{aligned} P(-0.5 < x < 0.5) \\ = \int_{-0.5}^{0.5} \frac{1}{\sigma \sqrt{2\pi}} \left(-\frac{(x - bias)^2}{2\sigma^2} \right) dx \end{aligned} \quad (38)$$

where $bias$ represents mean bias and it is considered to be 0.

It should be noted that considering AR performance of NL ambiguity is sensitive to various noises, under the assumption that the DD eliminates the ionosphere delay, the ionosphere delay actually exists although it is small. It is necessary to select the NL combination with a small ISF as much as possible to reduce the negative effects of ionospheric delay. For example, the (4.0-3) in Table 2 is an ideal NL combination due to the ISF is only 0.2.

2.3.2. Overview of BDS/MEMS-IMU Loosely-Coupled Integration System. In order to improve the real-time performance of the integrated system, the proposed algorithm adopt the loosely-coupled form with a small amount of computation. In the BDS triple-frequency AR process, PNF is used to reduce the total noise level of NL observations to improve the ambiguity fixed reliability.

Figure 1 shows the overall block diagram of the proposed algorithm. The blue EWL, WL, and NL represent ambiguity-unfixed combination observations, the gray EWL, WL, and NL represent ambiguity-fixed combination observations. The NL' represents the NL observation after the total noise level is reduced. The r_{BDS} can only be input to the EKF after the coordinate system is converted. Similarly, the results of EKF must be converted through the coordinate system to calculate ρ_{INS} .

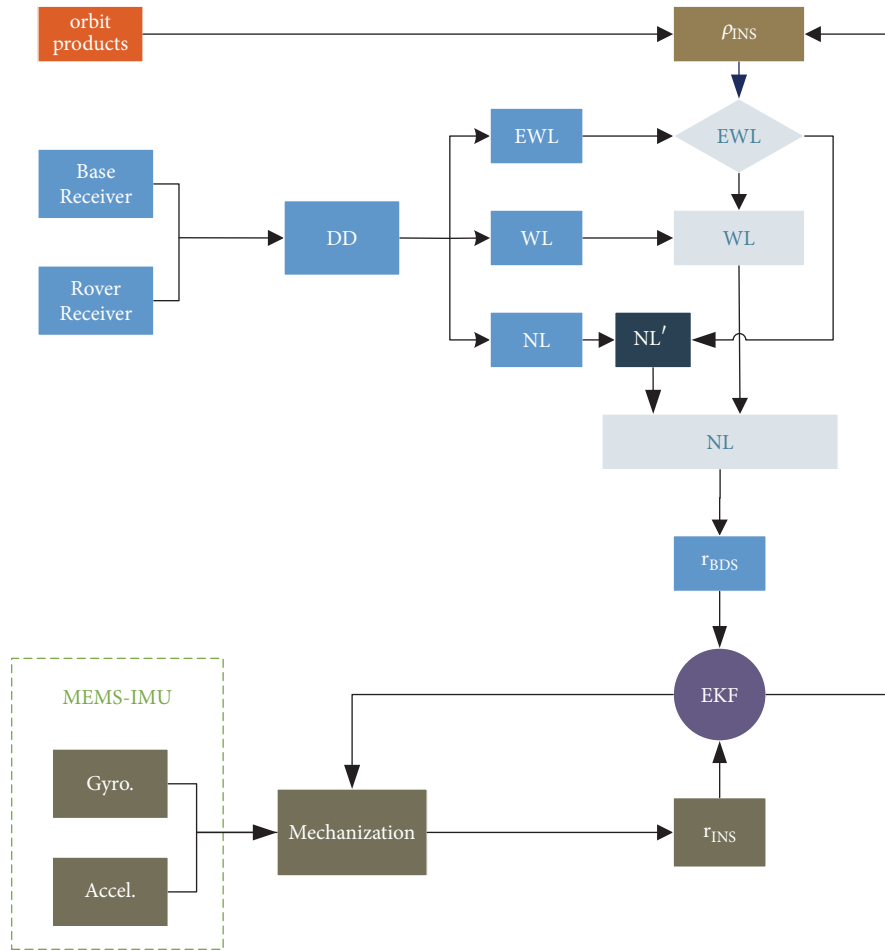


FIGURE 1: Overview of BDS/INS loosely-coupled integration system.

3. Data

In order to evaluate the performance of the proposed MEMS-IMU assisted BDS triple-frequency AR method, the field vehicular experiment of the integrated navigation system was conducted in Taiyuan, China, on June 6, 2018, from 9:30 to 10:30 am. The MEMS-grade INS and BDS rover receivers are installed on the top of the experimental vehicle to collect data on the test road with a sampling interval 1s. The entire test road can be divided into three types according to the characteristics of the road environment: open sky, urban canyon and roadside trees. The most serious occlusion and reflection of satellite signals is the urban canyon section, and the signal blockage of the roadside tree section is not serious, and the signal of the open sky road section is completely unobstructed. The speed of the experimental vehicle is maintained at about 5m/s, the baseline length of the entire experimental road is within 5km, and the data collection time is 1 hour. Figure 2 shows the map of the experimental area, the blue line is the trajectory of the experimental vehicle, and the red point marked “BASE” is the installation position of the BDS base receiver on the roof of a library. The places marked with “START” and “END” are the starting and ending points of the driving route of the experimental vehicle.

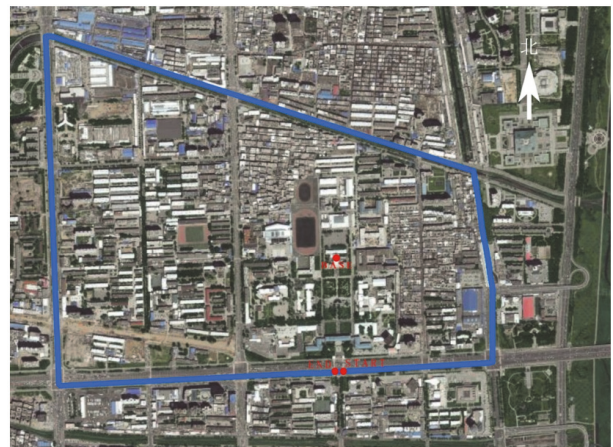


FIGURE 2: Experimental area and vehicle trajectory.

The POS1100 MEMS-grade INS was used in the experiment and included three MEMS gyroscopes and three quartz accelerometers. The coordinate parameters of the vehicle trajectory in the map are measured in advance using a tactical-grade INS POS310. Both of the two IMUs are provided by

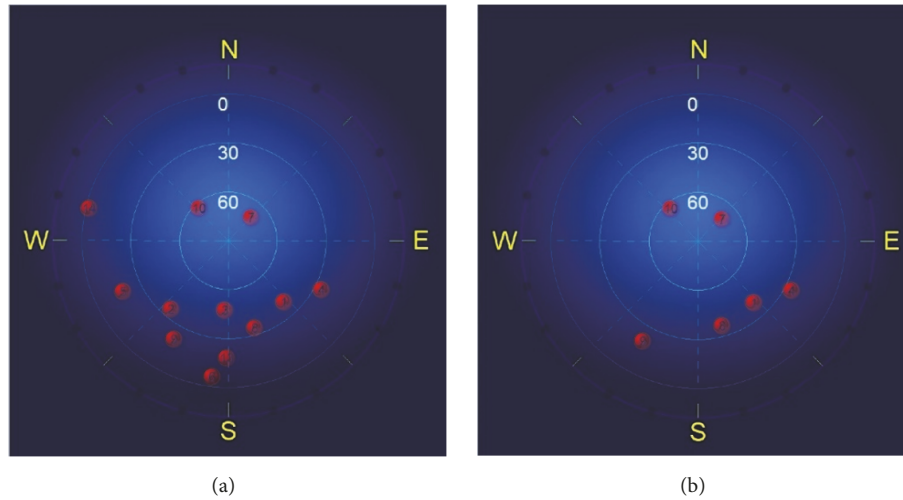


FIGURE 3: Received BDS satellites. (a) The 2th period and (b) the 6th period.

Wuhan MaiPu Space Time Technology Company (Wuhan, China). Their main performance specifications are shown in Table 2.

The BDS base station receiver UR380 installed on the roof of the library, and the BDS Rover receiver UB4B0 installed on experimental vehicle. Both of the BDS receivers that can receive and process triple-frequency observations are provided by Unicore Communications, Inc. (Beijing, China).

4. Results and Discussion

4.1. The Influence of Complex Environments on Observations.

In order to analyze the influence of different road environments on the observations, the entire test data is divided into 10 periods on average according to the length of time, each for 6 minutes (360 epochs). The 2th period (9:36-9:42) belongs to the open sky road section without any occlusion, and the 6th period (10:00-10:06) belongs to the urban canyon road section with severe occlusion. Only the data of these two periods of the extreme environment are selected for comparative analysis. Figure 3 shows the received BDS satellites in the 2th period and the 6th period.

The BDS includes geostationary earth orbit (GEO), Inclined Geosynchronous Satellite Orbit (IGSO), and Medium Earth Orbit (MEO) satellites. Tables 3 and 4, respectively, list the satellite types and elevation angles during the 2th and 6th periods.

Comparing Tables 3 and 4, it can be seen that the number of visible satellites in the 6th period is significantly less than that in the 2th period.

The occlusion or reflection of the BDS signal not only leads to a reduction in the number of visible satellites, but also a multipath error that reduces the accuracy of the observations, especially pseudoranges. Figure 4 illustrates the code multipath errors of visible satellites at B1, B2, and B3 in the 2th and 6th periods.

For short baselines, the DD eliminates most of the errors, and code multipath error becomes the main error affecting the AR performance. By comparing the pictures in the top

and bottom rows in Figure 4, the code multipath error in the 2th period is obviously smaller than that in the 6th period. The code multipath at B1 and B2 is only about 0.5m in the 2th period, while most of them are about 2m, and some epochs are even up to 4m in the 6th period, the situation of B3 is similar to that of B1 and B2. The pseudorange with such large code multipath error is difficult to fix the EWL ambiguity by the rounding. This means that the signal is occluded, which reduces the accuracy of the pseudorange and the AR performance.

Further observation shows that the code multipath error at B3 is generally less than that at B1 and B2, This is because the B3 has a chip rate of 10.23 Mcps and the accuracy of chip is relatively high. In addition, the code multipath error of the C09 satellite is significantly higher than that of other satellites. It can be seen from the comparison that the elevation angle of the C09 satellite is relatively low, indicating that the satellite elevation angle is directly related to the code multipath error.

4.2. MEMS-IMU Fixed EWL Ambiguity. In order to fully prove that MEMS-IMU can improve the AR performance of EWL ambiguity, three different TCAR methods are compared with the proposed method. The data of 10 periods are processed by four TCAR methods. The AR performance indicator uses the fixed success rate and the time to first fix (TTFF). The four methods for fixing the EWL ambiguity are as follows:

Scheme A: GF-TCAR, which is described in Section 2.1.2.

Scheme B: GB-TCAR, integer least squares model based on geometry.

Scheme C: GIF-TCAR, in addition to the GIF condition, the triple-frequency pseudorange observations together fix the EWL ambiguity.

Scheme D: INS-TCAR, the proposed method.

The cut-off elevation angle is set to 10° , and C07 satellite is used as the pivot satellite throughout the experiment.

4.2.1. Fixed Success Rate of EWL Ambiguity. The ambiguity fixed success rate is one of the commonly used indicators

TABLE 2: The main performance parameters of the two INS.

IMU	Grade	Gyro.(°/h)	Acce. (mGal)	Output(Hz)	Dimension(mm)
POS310	Tactical	0.5	25	200	151 × 120 × 101
POS1100	MEMS	10.0	2000	200	81.8 × 68 × 70

TABLE 3: Relevant parameters of visible satellites during the 2th period.

Orbit Type	GEO	GEO	GEO	GEO	GEO	IGSO
PRN	C01	C02	C03	C04	C05	C06
Elev. (°)	43	37	48	24	16	9
Orbit Type	IGSO	IGSO	IGSO	IGSO	IGSO	MEO
PRN	C07	C08	C09	C10	C13	C14
Elev. (°)	70	33	18	64	16	4

TABLE 4: Related parameters of visible satellites during the 6th period.

Orbit Type	GEO	GEO	IGSO	IGSO	IGSO	IGSO
PRN	C01	C04	C07	C08	C09	C10
Elev. (°)	40	24	68	33	16	62

for measuring AR performance. Figure 5 shows the EWL ambiguity fixed success rate with four different schemes over 10 periods.

As can be seen from Figure 5, scheme D has a fixed success rate of nearly 100% in 10 periods, while the fixed success rates of the other three schemes vary with different periods, and the fixed success rates of the three schemes are lower than scheme D. This is because the MEMS-IMU cannot only outputs high-precision positioning parameters but also is not affected by the external environment. The first three schemes of fixing the EWL ambiguity with pseudoranges, because the accuracy of the pseudorange is affected by the multipath error caused by the external environment, the fixed success rate is smaller than the scheme D in each period, especially the sixth time period, the fixed success rate of the first three schemes is less than 80%. In addition, the success rate of scheme B and C is higher than that of scheme A. This is because the integer least squares method has better AR performance than the rounding method as the number of epochs is accumulated. The GIF model completely eliminates the ionospheric and tropospheric delay errors, and can also improve the EWL ambiguity fixed success rate.

4.2.2. TTFF of EWL Ambiguity. TTFF refers to the time it takes for the ambiguity to be correctly fixed for the first time. It can reflect the real-time performance of ambiguity fixation and positioning. Figure 6 shows the TTFF of four different TCAR methods in 10 periods.

It can be seen from Figure 6 that the TTFF of scheme D is much smaller than the first three schemes, and even in the 2th period of open sky, the TTFF of scheme D is much shorter than the first three schemes. This is because the MEMS-IMU not only provides high-precision positioning parameters, but also has an output frequency of up to 200 Hz. It should be noted that the TTFF of scheme C is smaller than scheme B,

which may be the triple-frequency pseudorange increases the multipath error.

4.3. Reliable Fixation of NL Ambiguity. In order to prove that the proposed method can solve the problem that NL ambiguity is difficult to be fixed in a complex environment, we use scheme D to process and analyze the data of the 6th period with the largest multipath error. Only the ambiguities of EWL, WL, and NL are all fixed correctly to obtain BDS high-precision positioning results. Failure to fix the ambiguity not only reduces the positioning accuracy of the BDS but also does not correct the cumulative error of the MEMS-IMU. Figure 7 shows the ambiguity fixed success rate for scheme D before and after the reduction in the total noise level of the NL observations.

As can be seen from Figure 7, the fixed success rate of EWL and WL ambiguities for each available satellite is relatively high, close to 100%, while the NL ambiguities are all relatively low, all below 80%, and C09 satellite even below 60% due to the low elevation angle. This is because MEMS-IMU provides high-quality prior information for the fixation of EWL and WL ambiguities and the observation wavelengths of EWL and WL are large, which not only accelerates the fixing of EWL ambiguity but also improves the ambiguity fixed success rate of the EWL and WL. The phase multipath and unmodeled (ionosphere and tropospheric delay) errors in complex environments are amplified by DD and linear combination. The error is relatively larger than the NL observation wavelength, and the NL ambiguity is difficult to be fixed reliably. According to formulas (36) and (37), the phase noise variance of NL observations is obtained from ambiguity-fixed EWL observation to reduce the total noise level of the NL observations. Figure 8 shows that NL float ambiguity before and after the total noise level is reduced for each available satellite.

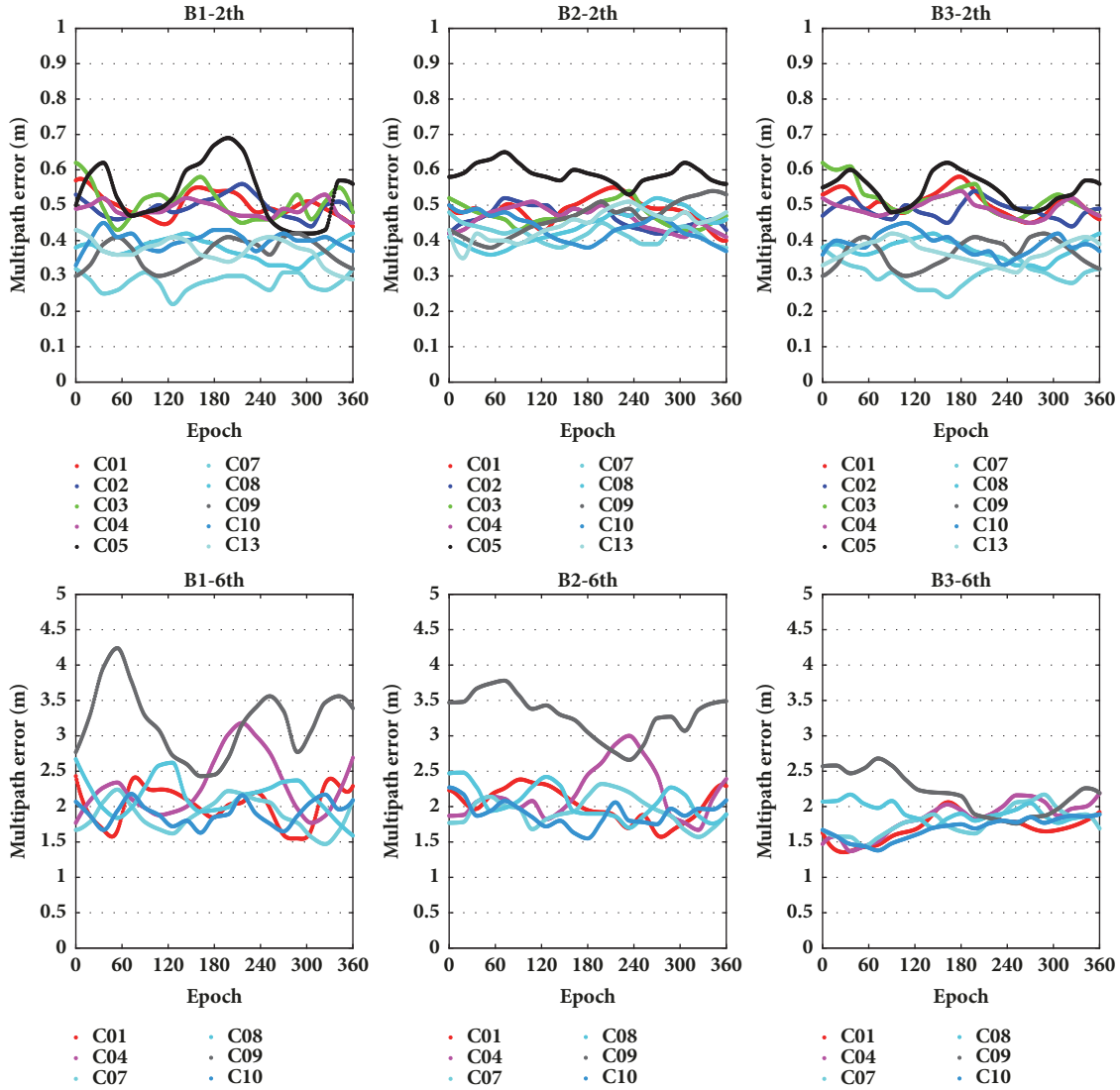


FIGURE 4: Code multipath error at three frequency in the 2th period (top) and the 6th period (bottom).

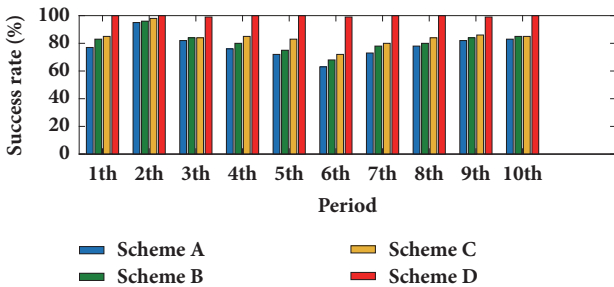


FIGURE 5: EWL ambiguity fixed success rate of Scheme A (blue), Scheme B (green), Scheme C (yellow), and Scheme D (red) in 10 periods.

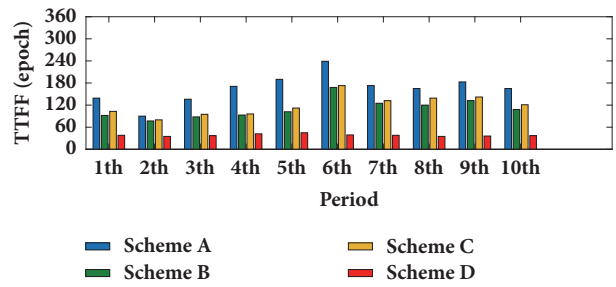


FIGURE 6: TTFF of the four TCAR in 10 periods.

From the first and the third rows of Figure 8, we can see that the residual between float ambiguity and corresponding integer ambiguity for each available satellite is relatively large, many epochs are greater than half cycles, and some are

even more than a cycle. Therefore, NL ambiguity cannot be reliably fixed by rounding. This is mainly due to the fact that the NL observations have short wavelengths and are subject to various noise pollution including phase multipath in a complex environment.

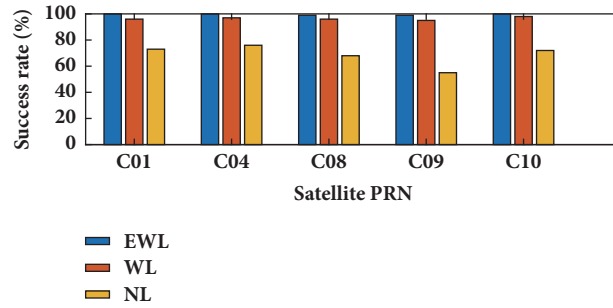


FIGURE 7: Ambiguity fixed success rate before the total noise level of the NL observation is reduced.

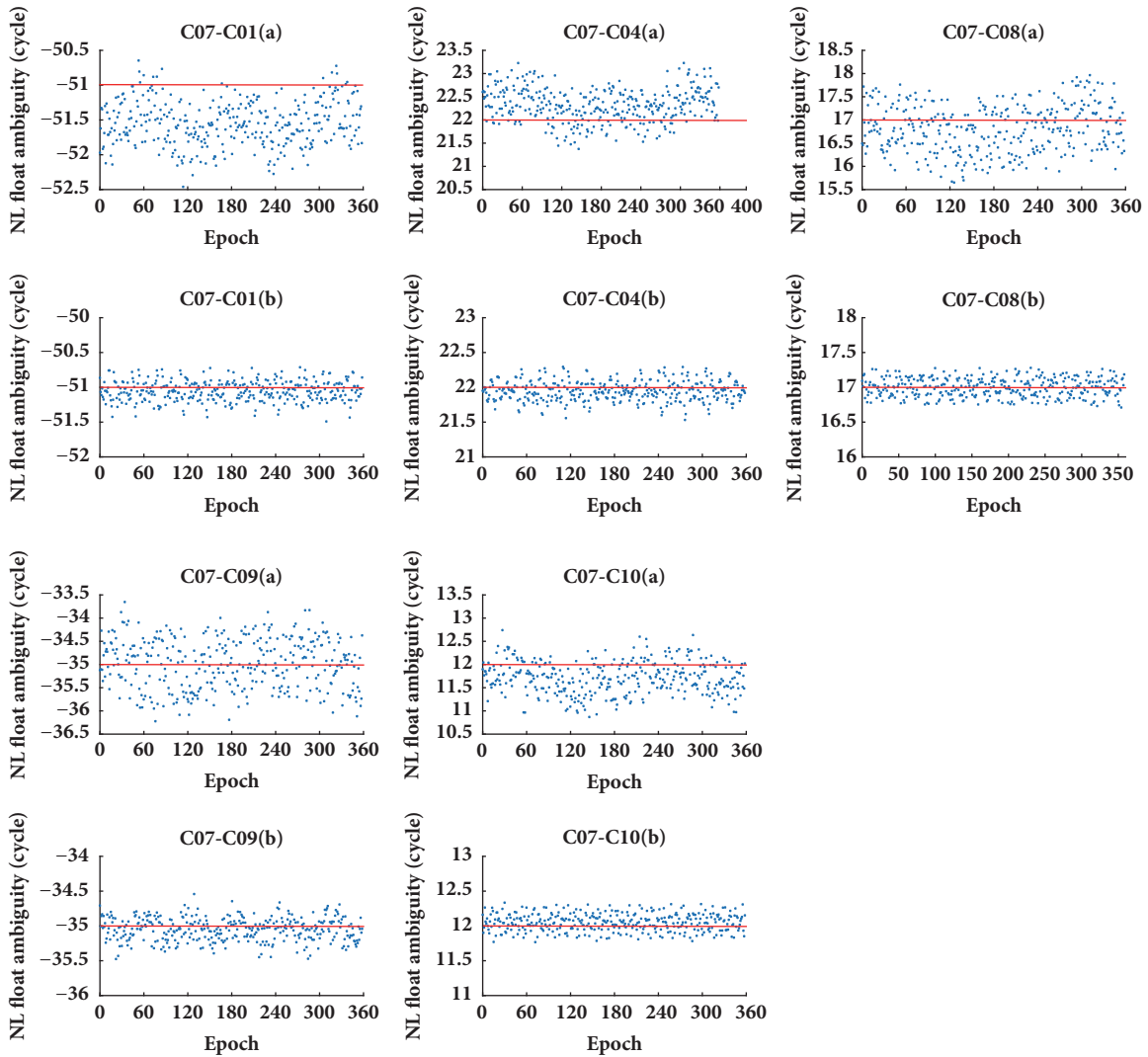


FIGURE 8: NL float ambiguity before (a) and after (b) the total noise level is reduced.

It can be seen from the second and fourth rows of Figure 8 that the residuals are significantly reduced, all less than half a cycle, and some even less than 0.2 cycles. Such high precision float ambiguity ensures that the NL ambiguity can be reliably fixed. Figure 9 shows fixed success rate of NL ambiguity before and after the total noise level is reduced.

It can be seen from Figure 9 that after the total noise level is reduced, the fixed success rate of the NL ambiguity is greatly improved. This is because the error of the ionosphere and tropospheric delay has been basically eliminated by DD, and the noise including the phase multipath error becomes the main error source. Therefore, the total noise level is greatly

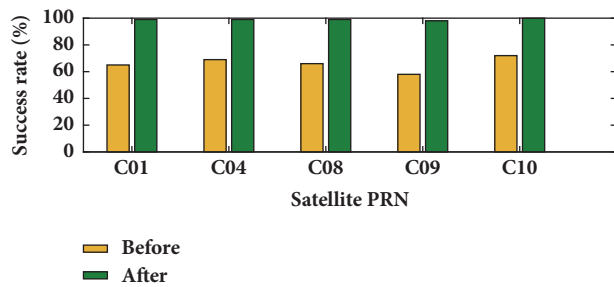


FIGURE 9: Fixed success rate of NL ambiguity before and after the total noise level is reduced.

reduced, and the fixed success rate of NL ambiguity is also greatly improved.

5. Conclusion and Outlook

In the open sky environment, the traditional TCAR and its derivative algorithms have fast and reliable AR performance due to the high quality BDS triple-frequency observations. However, in complex environments, satellite signals are blocked or reflected by obstacles causing severe multipath errors in pseudorange and carrier phase observations. To solve this problem, it is proposed to use the MEMS-IMU corresponding geometric distance instead of pseudorange to fix EWL ambiguity. Then, the noise variance of the NL observation is obtained from the EWL observation to reduce the total noise variance and improve the reliability of the NL ambiguity fixed. MEMS-IMU can output high-quality positioning parameters at high frequency in a short time; it not only improves the BDS AR success rate, but also improves the stability and continuity of BDS positioning, especially in the tunnel. The BDS positioning results can then be used to correct the cumulative error of the MEMS-IMU; both are loosely coupled by EKF.

The field vehicular experiment experiments were conducted on urban streets to verify the feasibility of the proposed algorithm. The result proves that the proposed algorithm not only speed up the fixation of the ambiguity through the combination of MEMS-IMU and BDS triple-frequency but also improves the reliability of the fixed ambiguity.

The proposed method is mainly to improve the AR performance for the short baseline in complex environments. For the medium-to-long baseline, the temporal and spatial correlation of observations is reduced, and ionospheric delays cannot be eliminated by DD. It is necessary to analyze the characteristics of various error sources and propose an effective algorithm.

Data Availability

The data used to support the findings of this study are available from the corresponding author upon request.

Conflicts of Interest

The authors declare no conflicts of interest.

Authors' Contributions

Junbing Cheng and Dengao Li conceived and designed the experiments; Junbing Cheng performed the experiments; Junbing Cheng and Jumin Zhao analyzed the data; Junbing Cheng wrote the paper; Dengao Li critically reviewed the paper.

Acknowledgments

This work is partially supported by the National High Technology Research and Development Program ("863" Program) of China with Grant no. 2015AA016901, partially sponsored by the General Object of National Natural Science Foundation with two Grant nos. 61772358 and 61572347, partially by a project funded by the International Cooperation Project of Shanxi Province with Grant no. 201603D421012.

References

- [1] X. He, X. Zhang, L. Tang, and W. Liu, "Instantaneous real-time kinematic decimeter-level positioning with BeiDou triple-frequency signals over medium baselines," *Sensors*, vol. 16, 2016.
- [2] K. M. Pesyna, T. E. Humphreys, R. W. Heath, T. D. Novlan, and J. C. Zhang, "Exploiting antenna motion for faster initialization of centimeter-accurate gnss positioning with low-cost antennas," *IEEE Transactions on Aerospace and Electronic Systems*, vol. 53, no. 4, pp. 1597–1613, 2017.
- [3] P. J. G. Teunissen, "The least-squares ambiguity decorrelation adjustment: a method for fast GPS integer ambiguity estimation," *Journal of Geodesy*, vol. 70, no. 1-2, pp. 65–82, 1995.
- [4] P. J. G. Teunissen, R. Odolinski, and D. Odijk, "Instantaneous BeiDou+GPS RTK positioning with high cut-off elevation angles," *Journal of Geodesy*, vol. 88, no. 4, pp. 335–350, 2014.
- [5] R. Odolinski and P. J. G. Teunissen, "Low-cost, high-precision, single-frequency GPS-BDS RTK positioning," *GPS Solutions*, vol. 21, no. 3, pp. 1315–1330, 2017.
- [6] A. Brack, "Reliable GPS + BDS RTK positioning with partial ambiguity resolution," *GPS Solutions*, vol. 21, pp. 251–264, 2017.
- [7] A. Parkins, "Increasing GNSS RTK availability with a new single-epoch batch partial ambiguity resolution algorithm," *GPS Solutions*, vol. 15, no. 4, pp. 391–402, 2011.
- [8] W. Tang, C. Deng, C. Shi, and J. Liu, "Triple-frequency carrier ambiguity resolution for Beidou navigation satellite system," *GPS Solutions*, vol. 18, no. 3, pp. 335–344, 2014.
- [9] W. Gao, C. Gao, S. Pan, D. Wang, and J. Deng, "Improving ambiguity resolution for medium baselines using combined GPS and BDS Dual/triple-frequency observations," *Sensors*, vol. 15, no. 11, pp. 27525–27542, 2015.
- [10] M. Cocard, S. Bourgon, O. Kamali, and P. Collins, "A systematic investigation of optimal carrier-phase combinations for modernized triple-frequency GPS," *Journal of Geodesy*, vol. 82, no. 9, pp. 555–564, 2008.
- [11] B. Forssell, M. Martin-Neira, and R. Harrisz, "Carrier phase ambiguity resolution in GNSS-2," in *Proceedings of the ION GPS-97*, pp. 1727–1736, Kansas City, Mo, USA, 1997.
- [12] U. Vollath, S. Birnbach, H. Landau et al., "Analysis of three-carrier ambiguity resolution (TCAR) technique for precise relative positioning in GNSS-2," in *Proceedings of the ION GPS*, pp. 417–426, 1998.

- [13] R. Hatch, J. Jung, P. Enge, and B. Pervan, "Civilian GPS: the benefits of three frequencies," *GPS Solutions*, vol. 3, no. 4, pp. 1–9, 2000.
- [14] Y. Feng, "GNSS three carrier ambiguity resolution using ionosphere-reduced virtual signals," *Journal of Geodesy*, vol. 82, no. 12, pp. 847–862, 2008.
- [15] B. Li, Y. Feng, and Y. Shen, "Three carrier ambiguity resolution: Distance-independent performance demonstrated using semi-generated triple frequency GPS signals," *GPS Solutions*, vol. 14, no. 2, pp. 177–184, 2010.
- [16] Q. Zhao, Z. Dai, Z. Hu, B. Sun, C. Shi, and J. Liu, "Three-carrier ambiguity resolution using the modified TCAR method," *GPS Solutions*, vol. 19, no. 4, pp. 589–599, 2015.
- [17] Y. Tian, D. Zhao, H. Chai, and S. Wang, "BDS ambiguity resolution with the modified TCAR method for medium-long baseline," *Advances in Space Research*, vol. 59, no. 2, pp. 670–681, 2017.
- [18] Y. Lou, X. Gong, S. Gu, F. Zheng, and Y. Feng, "Assessment of code bias variations of BDS triple-frequency signals and their impacts on ambiguity resolution for long baselines," *GPS Solutions*, vol. 21, no. 1, pp. 177–186, 2017.
- [19] C. Deng, W. Tang, J. Cui et al., "Triple-frequency code-phase combination determination: A comparison with the Hatch-Melbourne-Wübbena combination using BDS signals," *Remote Sensing*, vol. 10, no. 2, article 353, 2018.
- [20] F. Chu and M. Yang, "BeiDou System (BDS) Triple-Frequency Ambiguity Resolution without Code Measurements," *Remote Sensing*, vol. 10, no. 5, article 675, 2018.
- [21] C. Zhang, X. Li, S. Gao, T. Lin, and L. Wang, "Performance analysis of global navigation satellite system signal acquisition aided by different grade inertial navigation system under highly dynamic conditions," *Sensors*, vol. 17, no. 5, article 980, 2017.
- [22] D. A. Grejner-Brzezinska, R. Da, and C. Toth, "GPS error modeling and OTF ambiguity resolution for high-accuracy GPS/INS integrated system," *Journal of Geodesy*, vol. 72, no. 11, pp. 626–638, 1998.
- [23] S. Godha and M. E. Cannon, "GPS/MEMS INS integrated system for navigation in urban areas," *GPS Solutions*, vol. 11, no. 3, pp. 193–203, 2007.
- [24] S. Liu, F. Sun, L. Zhang, W. Li, and X. Zhu, "Tight integration of ambiguity-fixed PPP and INS: model description and initial results," *GPS Solutions*, vol. 20, no. 1, pp. 39–49, 2016.
- [25] H. Han, J. Wang, J. Wang, and A. H. Moraleda, "Reliable partial ambiguity resolution for single-frequency GPS/BDS and INS integration," *GPS Solutions*, pp. 1–14, 2016.
- [26] T. Li, H. Zhang, Z. Gao, Q. Chen, and X. Niu, "High-accuracy positioning in urban environments using single-frequency multi-GNSS RTK/MEMSIMU integration," *Remote Sensing*, vol. 10, no. 2, article 205, 2018.
- [27] S. Sasani, J. Asgari, and A. R. Amiri-Simkooei, "Improving MEMS-IMU/GPS integrated systems for land vehicle navigation applications," *GPS Solutions*, vol. 20, no. 1, pp. 89–100, 2016.
- [28] J. Moreau, S. Ambellouis, and Y. Ruichek, "Fisheye-based method for GPS localization improvement in unknown semi-obstructed areas," *Sensors*, vol. 17, no. 1, article 119, 2017.
- [29] R. Moradi, W. Schuster, S. Feng, A. Jokinen, and W. Ochieng, "The carrier-multipath observable: a new carrier-phase multipath mitigation technique," *GPS Solutions*, vol. 19, no. 1, pp. 73–82, 2014.
- [30] D. Donaldo and B. Benson, "A Comparison of Two Approaches to Pure-Inertial and Doppler-Inertial Error Analysis," *IEEE Transactions on Aerospace and Electronic Systems*, vol. 11, no. 4, pp. 447–455, 1975.
- [31] K.-W. Chiang, T. T. Duong, and J.-K. Liao, "The performance analysis of a real-time integrated INS/GPS vehicle navigation system with abnormal GPS measurement elimination," *Sensors*, vol. 13, no. 8, pp. 10599–10622, 2013.
- [32] B. Li, S. Verhagen, and P. J. G. Teunissen, "Robustness of GNSS integer ambiguity resolution in the presence of atmospheric biases," *GPS Solutions*, vol. 18, no. 2, pp. 283–296, 2014.

